2020 IEEE International Conference on Robotics and Automation (ICRA)
31 May - 31 August, 2020. Paris, France

SNIAE-SSE Deformation Mechanism Enabled Scalable Multicopter: Design, Modeling and Flight Performance Validation

Tao Yang, Yujing Zhang, Peng Li, Yantao Shen, Yunhui Liu and Haoyao Chen

***Abstract*—This paper focuses on designing, modeling and validating a novel scalable multicopter whose deformation mechanism, called SNIAE-SSE, relies on a combination of simple non-intersecting angulated elements (SNIAEs) and straight scissor-like elements (SSEs). The proposed SNIAE-SSE mechanism has the advantages of single degree-of-freedom, fast actuation capability and large deformation ratio. In this work, enabled by the SNIAE-SSE mechanism, a quadcopter prototype with symmetrical and synchronous deformation is firstly developed, which facilitates a novel and controllably scalable multicopter system for us to analyze its modeling, as well as to validate its flight performance and dynamics during the deformation in several flight missions including hover, throwing, and morphing flying through a narrow window. Experimental results demonstrate that the developed scalable multicopter can maintain its stable flight behavior even both the folding and unfolding body deformations are fast performed, which indicates an excellent capability of the scalable multicopter to rapidly adapt to complex and dynamically changed environments.**

I. Introduction

As reported, large multicopters can stably fly and perform aerial tasks due to their significant torque output and balance capability, while small multicopters with highly flexible maneuverability allow them to rapidly travel through narrow spaces [1, 2]. The both advantages of two-scale mechanisms are rarely found in a conventional multicopter, so there is a demand that a scalable multicopter owning the advantages from varied scale mechanisms thereby has capabilities to adapt to multiple flight conditions and to fulfill various tasks.

To date, several techniques have been reported to attempt achieving the multiple scales of multicopter through deformability. For instance, a self-deploying quadcopter presented in [3] can quickly unfold its arms with the aid of the torque generated by propellers during takeoff, and a quadcopter described in [4] is able to fold its arms using an extra actuator and unfold its arms automatically utilizing its origami structure's spring effect during the flight. Both above mentioned foldable multi-rotors rely on an origami based deformation mechanism. The deformation mechanism however has a limited stiffness, and it doesn't allow for a larger deformation ratio as well. In addition, there exists another popular way to change body configurations of multicopters using the rotationally folding/pulling the propellers/arms. The foldable quadcopter introduced in [5] can drive its propellers to rotate around the arms for reaching a vertical flight mode configuration. The quadcopter depicted in [6] uses a servomotor to rotate its propellers in order to change the wingspan of the copter, and relying on the equipped springs to passively pull the arms when the rotors speed are reduced, a quadcopter in [7] can deform into a folded configuration for the purpose of passing through a narrow gap. These mechanisms help reduce the size of multicopters in one or two dimensions, but meanwhile it will increase the size in another dimension, which results in achieving partial deformation that limits their adaptation to flight environments. One interesting work presented in [8] facilitates four rotor arms to rotate independently around the main body frame so as to adjust flight mode configurations during the flight. Based on its technical description, the deformation ratio of the whole frame is limited and is hard to be applied for a scalable mechanism with multiple rotor arms. Recently a deformable quadcopter was proposed in [9] by the author, it was designed with an actuated scissor-like morphing structure that is capable of enabling a symmetrical deformation of whole body frame. It however needs a long guide rail to support the morphing structure, which reduces the deformation ratio and downgrades its fast actuation capability in certain degree due to the induced mechanical constraints and frictions.

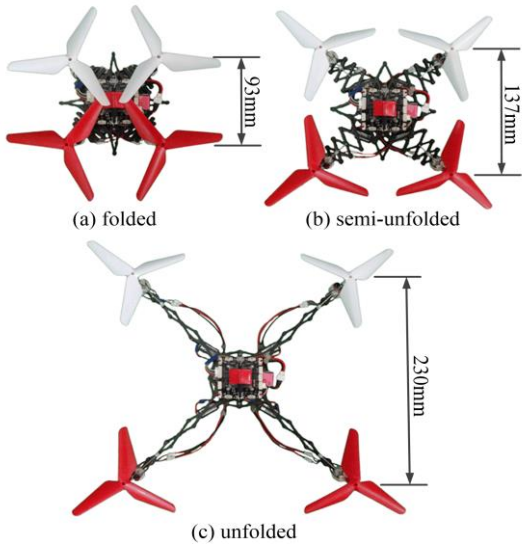

Figure 1. SNIAE-SSE deformation mechanism enabled scalable multicopter in three typical configurations. (a) Full folded configuration. (b) Semi-unfolded configuration. (c) Unfolded configuration.

In this work, we address to develop a deformation enabled scalable multicopter with fast actuation capability and large deformation ratio, so as to enhance its flight adaptability to complex environments and to facilitate multiple task-oriented

T. Yang and Y. Zhang are graduate students with HIT Shenzhen, China (yangtao@stu.hit.edu.cn).

P. Li and H. Chen are with HIT Shenzhen, China（peng.li@hit.edu.cn）
and Li's work was partially supported by JCYJ20180507183456108 and Chen's work was partially supported by the National Natural Science Foundation of China under Reference No. U1713206.

Y. Shen is with University of Nevada, Reno, NV 89557, USA.

Y. Liu is with the Chinese University of Hong Kong, China.

versatility of such multicopter. As the scissor-like morphing mechanisms have the advantages of large-scale deformation, good structural stability, high efficiency of force transmission and strong maneuverability [10], and further inspired by mechanisms from both non-intersecting angulated element [11-13] and straight scissor-like element, we propose and design a high-performance scissor-like deformation mechanism that well leverages the simple non-intersecting angulated elements (SNIAEs) with the straight scissor-like elements (SSEs), called SNIAE-SSE. The SNIAE-SSE is capable of allowing one degree-of-freedom (DOF) and fast actuation and yet large deformation ratio. These properties suggest it is an excellent deformation candidate that enables a high-performance scalable multicopter. Note that, the proposed SNIAE-SSE is different from the deformation mechanism for the quadcopter mentioned in [9] as it doesn't need any long constrained guide rails for the support. It therefore promotes large deformation ratio and fast actuation capability of the scalable multicopter. In addition, due to the nature of stable, symmetrical and synchronous deformation of the SNIAE-SSE mechanism, it thus has less influences to multicopter dynamics, making the multicopter be able to stably fly even a fast folding and unfolding body deformations are performed during the flight, which indicates its excellent capability to rapidly adapt to complex and dynamically changed environments.

To validate the performance of the mechanism, a quadcopter prototype is firstly developed. Its several typical folding configurations are demonstrated in Figure 1. Relying on this prototype, the dynamic characteristics in different flight missions: (1) hover, (2) throwing, and (3) morphing flying through a narrow window are preliminarily validated. The remainder of this paper is organized as follows. Section II presents the mechanical design of our scalable multicopter. Section III analyzes the dynamics model of the scalable copter. Section IV validates the dynamic characteristics of the prototype. Section V concludes the work.

II. Deformation Mechanism and Copter Design

A. SNIAE-SSE Mechanism and Deformation Ratio

Using common scissor-like structures, i.e. the Hoberman's angulated element [14] and/or SSE, it is difficult to synthesize an overall deformation of the body frame for the goal of scalable multicopters. To reach the goal, here a new scissor-like deformation mechanism, called simple non-intersecting angulated element (SNIAE), is firstly introduced. The mechanism consists of a pair of different angulated rods connected by a revolute joint E and also enclosed an angle α in the middle, as illustrated in Figure 2. In Figure 2(b) terminal points A, B, C, D are constrained and can move along their dashed lines. To ensure the mobilization, the triangles AEB and DEC should both be isosceles, i.e. $AE = BE$, $CE = DE$. Here, $\angle AED$ and $\angle BEC$ are defined as ϕ and θ, respectively. Figure 2 shows the EF and EG perpendicular to the dashed lines, which form a quadrilateral with OF and OG to help us derive the relationship between ϕ, θ and α. So it can be obtained as

$$\alpha + \angle FEG = \pi \tag{1}$$

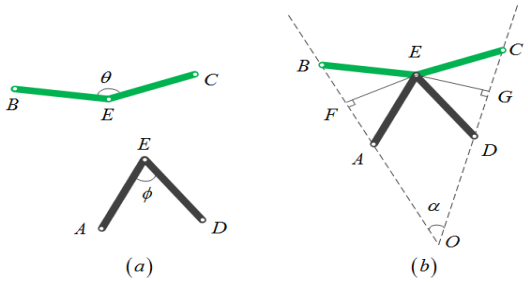

Figure 2. SNIAE consisting of a pair of different angulated rods. (a) Two angulated rods. (b) a SNIAE.

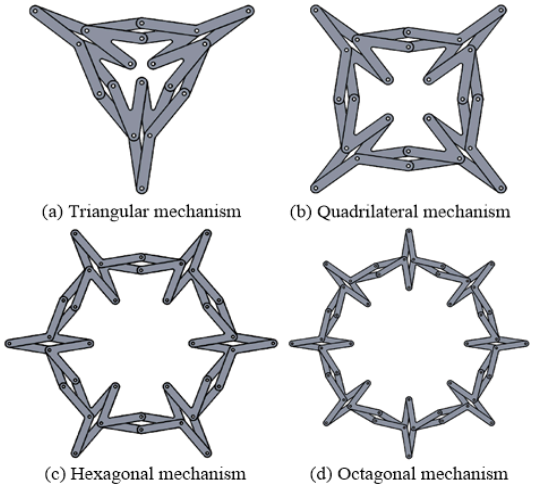

Figure 3. Standard closed-loop mechanisms. (a) Triangular mechanism containing three pairs of SNIAEs (n = 3). (b) Quadrilateral mechanism containing four pairs of SNIAEs (n = 4). (c) Hexagonal mechanism containing six pairs of SNIAEs (n = 6). (d) Octagonal mechanism containing eight pairs of SNIAEs (n = 8).

$\angle FEG$ can be rewritten as $\angle FEA + \phi + \angle DEG$, thus (1) can be re-described as

$$\angle FEA + \angle DEG = \pi - \alpha - \phi \tag{2}$$

Where $\angle FEA$ and $\angle DEG$ can be redefined as $\angle AEB/2$ and $\angle CED/2$, respectively. Substitute them into (2) gives

$$\angle AEB + \angle CED = 2(\pi - \alpha - \phi) \tag{3}$$

It then has the form as

$$\angle AEB + \phi + \angle CED + \theta = 2\pi \tag{4}$$

Substitute (3) into (4), the relationship between ϕ, θ and α can be derived as

$$\alpha = (\theta - \phi)/2 \tag{5}$$

Especially, when $AE = BE = CE = DE$, $\phi + \theta = \pi$ is satisfied, any even number of identical SNIAEs interconnected at terminal points can form a series of standard closed-loop mechanisms, which can be folded to its most compact state and has only single DOF. It can be then found that

$$\alpha = \pi / n \qquad (n \geq 3, n \in \mathbb{N}) \tag{6}$$

Where n is the pair number of SNIAEs.

Based on SNIAE mechanism, several standard closed-loop foldable mechanisms are shown in Figure 3. Through incorporating one of the closed-loop mechanisms with any number of SSEs, a new SNIAE-SSE deformation mechanism can be well formed and designed. The deformation mechanism provides an excellent solution for designing the deformable body frame of scalable multicopters. Figure 4 demonstrates the SNIAE-SSE deformation mechanism for a scalable quadcopter. As displayed, it consists of a SNIAE quadrilateral mechanism and twelve SSEs that are evenly connected to four external endpoints of the quadrilateral mechanism to form the scalable arms of the quadcopter. The SNIAE's rods are designed with the same length l_0 and the lengths of SSE's rods are l_i ($i \in \{1, 2, 3\}$). The controlled servo angle is β, and the equivalent radius of the deformable body frame is R. In order to estimate the deformation ratio of the scalable copter conveniently, we assume that

$$l_i = l_0 \tag{7}$$

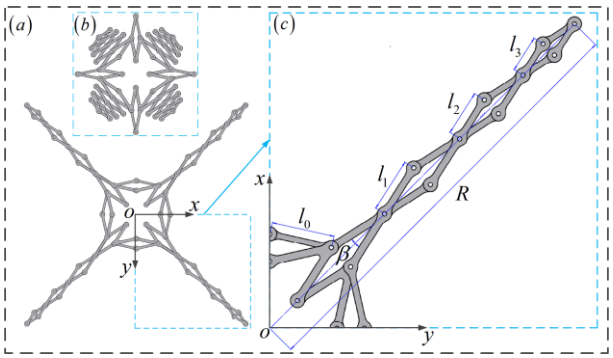

Figure 4. The deformation mechanism of the scalable quadcopter. (a) unfolded configuration. (b) folded configuration. (c) one scalable rotor arm of quadcopter.

For the scalable length of the rotor arm, it can be defined as

$$R = l_0 \left[\cos\frac{\beta}{2}\left(\frac{1}{\sin\left(\frac{\pi}{n}\right)} + 2m + 1 \right) + \sin\frac{\beta}{2}\cot\frac{\pi}{n} \right] \tag{8}$$

Where m is the number of SSEs per arm of a copter. In theory, if ignoring the width of the rods, the value of β should be satisfied with $\beta \in [0, \pi]$, and the minimum $R_{\min}$ of a copter arm occurs when $\beta = \pi$, namely

$$R_{\min} = l_0 \cot\frac{\pi}{n} \tag{9}$$

From (9), it can be seen that the minimum size of a copter (arm) is mainly affected by l_0 and n. When both l_0 and n are changed, the size of a copter is also varied.

The maximum $R_{\max}$ of a copter (arm) occurs when $\beta = \beta_0$, which can be calculated as follow:

$$\beta_0 = 2\arctan\left[\frac{\cos(\pi/n)}{(2m+1)\sin(\pi/n)+1} \right] \tag{10}$$

Then the deformation ratio r_d of a copter can be derived as below:

$$r_d = \frac{R_{\max}}{R_{\min}} = \frac{1}{\sin(\beta_0/2)} \tag{11}$$

Equations (10) and (11) indicate that the deformation ratio of a copter is not heavily related to l_0 and is mainly affected by n and m, the relationship of which can be found in Figure 5. The deformation ratio changes mainly with the change of the value of m and n. when the value of m is constant, the smaller the value of n is, the larger the deformation ratio is. This implies that tri-copter (If n = 3) has the biggest deformation ratio when the number of SSEs per rotor arm is equal. When the value of n is constant, the bigger the value of m is, the larger the deformation ratio. Theoretically speaking, the mechanism can be designed to allow the scalable copter with a large deformation ratio.

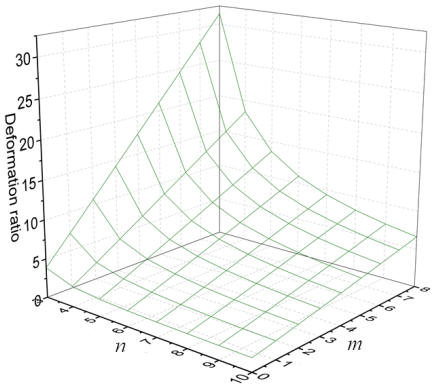

Figure 5. Deformation ratio of a scalable copter varying with m and n.

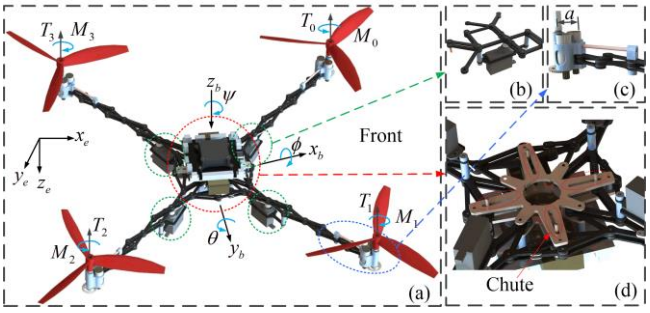

Figure 6. Scalable quadcopter. (a) unfolded configuration. (b) active unit consisting of servo motors and actuated scissor elements. (c) rotor mount with a very short guide shaft. (d) central body with four chutes.

B. Scalable (Deformable) Copter Design

Based on the SNIAE-SSE deformation mechanism, a scalable quadcopter is designed as shown in Figure 6. Except for nylon rotor mounts, the whole deformation mechanism is made of carbon fiber. Although the whole deformable quadcopter only has one DOF and can be driven by one servo motor to deform, in the design we still use four simultaneously driven small servomotors instead of a larger one in order to make the mass distribution of the quadcopter more uniform. Meanwhile, the adjacent servomotors rotate in opposite direction, which makes total torque on the body frame generated by the servomotors cancelled. In Figure 6(c), it

shows one of four rotor mounts with a very short guide shaft that ensures the rotor mount only moving along the axis of the arm when the arm is folded or unfolded. Figure 6(d) displays the central body with four chutes, which makes the body frame only folded and unfolded along the chutes. The design not only enables that the deformable quadcopter is symmetrically and synchronously deployed at any time in order to achieve the flight advantages traditional quadcopters have, but also adapts the copter to the changeable environment through the deformation.

III. Dynamics of the Deformable Multicopter

In this section we briefly describe the dynamics of the deformable quadcopter. The process can be extended to general scalable multicopters with the deformation mechanism.

A. Arm Length and Moment of Inertia

To model the copter, a world frame and a body frame are set up as shown in Figure 6(a). $\{x_e, y_e, z_e\}$ are the world frame, which is fixed during copter flight. The body frame $\{x_b, y_b, z_b\}$ will translate and rotate along with the copter. T_i and M_i ($i \in \{0, 1, 2, 3\}$) are the thrust and moment generated by i^{th} rotor, respectively. Different from the traditional quadcopter, the arm length and moment of inertia of a deformable copter will change during the deformation. A complete dynamics model can be achieved by deriving the dynamics model of the scalable rotor arms, and combining with the traditional flight dynamics model. The arm length of our scalable copter is denoted as $L(\beta)$, which can be seen from Figures 4(c) and 6(c) as below:

$$L(\beta) = R + a \tag{12}$$

Where a is the distance from the last revolute joint to rotor shaft, as shown in Figure 4(c).

To calculate the moment of inertia of the copter, a general method is to calculate the moment of inertia of each component and add them together to get the total moment of inertia. However, the scalable copter and its arms have very complex geometry and it results in a high computation load. To improve the computing efficiency, we used SOLIDWORKS Mass-Property toolbox to obtain the moment of inertia when the copter's arms are folded at different percentages to form the scalable copter. After conducting the cubic polynomial fitting on the computed data, the relationship between the controlled servo angle and moment of inertia can be found as described in eqn. (13). The related data and fitting results are plotted in Figure 7.

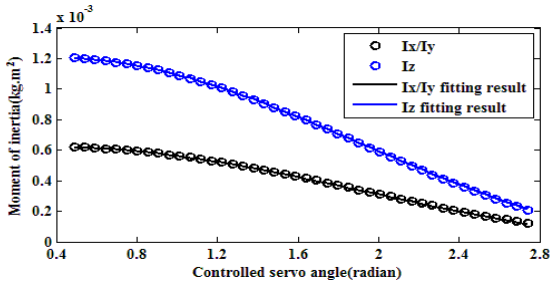

Figure 7. Fitting curves of moment of inertia with controlled servo angle.

$$\begin{cases} I_x(\beta) = I_y(\beta) = 10^{-5}\left(4.1\beta^3 - 24\beta^2 + 18\beta + 58.3\right) \\ I_z(\beta) = 10^{-5}\left(8.2\beta^3 - 47.7\beta^2 + 35.7\beta + 113.3\right) \end{cases} \tag{13}$$

Where $I_x(\beta)$, $I_y(\beta)$ and $I_z(\beta)$ are the moment of inertia of the copter along x_b, y_b and z_b axis, respectively.

B. Identification of Scalable Arm Dynamics

The arm length of the copter is controlled by four AF D30T-3.3 MG servomotors. To build the deformable arm dynamics, the system identification method is employed. Firstly, a high-speed motion capture system consisting of ten OPTITRACK cameras with 120Hz is employed to measure the step response data of one deformable copter's arm during hover. Then, with the system identification toolbox from MATLAB, we identified the scalable arm dynamics model of the copter during folding and unfolding respectively, as presented in eqn. (14). Figure 8 shows the comparison results on arm length between measured and simulated from the identified model. As plotted, the measured results agree with the values generated by the identified model very well.

$$\ddot{L}(\beta) = \begin{cases} -42.4\dot{L}(\beta) - 502.7L(\beta) + 505.8u_4 & folding \\ -13.2\dot{L}(\beta) - 76.9L(\beta) + 76.2u_4 & unfolding \end{cases} \tag{14}$$

Where u_4 is the command of the controlled servo angle.

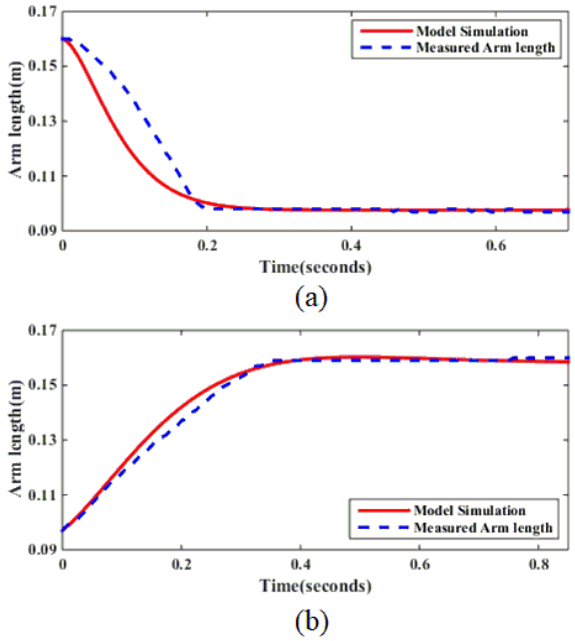

Figure 8. Comparison results on arm length between measured and simulated from the identified model. (a) Arm length in the folded process. (b) Arm length in the unfolded process.

C. Dynamics of the Scalable Copter

Taking into account the scalable arm length and its moment of inertia, the motion dynamics of the deformable quadcopter in translational and rotational movements can be obtained based on the Newton-Euler equations [15, 16], as listed in equation (15). Combining (14) with (15), we can have the described dynamics model of the scalable quadcopter.

$$\begin{cases} \ddot{x} = \frac{1}{m}\left[\left(\sin\phi\sin\psi + \cos\psi\sin\theta\cos\phi\right)u_0\right] \\ \ddot{y} = \frac{1}{m}\left[\left(\cos\phi\sin\psi\sin\theta - \cos\psi\sin\phi\right)u_0\right] \\ \ddot{z} = \frac{1}{m}\left[\left(\cos\phi\cos\theta\right)u_0\right] - g \\ \ddot{\phi} = \left(\frac{I_y(\beta) - I_z(\beta)}{I_x(\beta)}\right)\dot{\theta}\dot{\psi} - \frac{J_r}{I_x(\beta)}\dot{\theta}\Omega + \frac{L(\beta)}{\sqrt{2}I_x(\beta)}u_1 \\ \ddot{\theta} = \left(\frac{I_z(\beta) - I_x(\beta)}{I_y(\beta)}\right)\dot{\phi}\dot{\psi} + \frac{J_r}{I_y(\beta)}\dot{\phi}\Omega + \frac{L(\beta)}{\sqrt{2}I_y(\beta)}u_2 \\ \ddot{\psi} = \left(\frac{I_x(\beta) - I_y(\beta)}{I_z(\beta)}\right)\dot{\theta}\dot{\phi} + \frac{1}{I_z(\beta)}u_3 \end{cases} \quad (15)$$

Where m is the mass of the vehicle, g is the gravitational constant, J_r is the moment of inertia of the rotor. Ω is the sum of the rotating speed of four rotors. u_0 is the control input of the main thrust. u_1, u_2, and u_3 are used to control the movement of roll, pitch and yaw, respectively. To calculate u_i ($i \in \{0, 1, 2, 3\}$), the following equation can be applied:

$$\begin{bmatrix} u_0 \\ u_1 \\ u_2 \\ u_3 \end{bmatrix} = \begin{bmatrix} k_d & k_d & k_d & k_d \\ k_d & -k_d & -k_d & k_d \\ k_d & k_d & -k_d & -k_d \\ -k_b & k_b & -k_b & k_b \end{bmatrix} \begin{bmatrix} \omega_0^2 \\ \omega_1^2 \\ \omega_2^2 \\ \omega_3^2 \end{bmatrix} \quad (16)$$

Where k_d and k_b are the thrust constant and moment constant of the rotor respectively. ω_i ($i \in \{0, 1, 2, 3\}$) is the rotating speed of each rotor.

IV. Flight Dynamic Characteristics Validation

A. Scalable Copter Prototype and Set Up

The prototype of our scalable copter is illustrated in Figure 1, each arm consists of CNC-fabricated carbon fiber rods and a 3D-printed nylon rotor mount. The copter has a mass of 127g and an arm length that varies from 66 mm to 162.5 mm. The servomotors required for morphing have an overall weight of 20g, which corresponds to approximately 16% of the total weight of the prototype.

At the end of each arm, two 7×16mm 19000KV brushed motors drive a 3-blade, 120 mm propeller through a 1/4 gear reduction unit. The motors are controlled by a flight controller board. The flight controller board includes an Inertial Measurement Unit (IMU), a Barometer, and an Optical Flow Module. The Barometer allows the copter to fly at constant altitude, and the Optical Flow Module allows the copter to hover at a fixed point. In order to validate the dynamic characteristics of the deformable copter, we conducted the following flight behavior validation using the PID based flight controller [17, 18]: (1) hover, (2) throwing, and (3) morphing flying through a narrow window.

B. Hover

In this validation, the hovering experiments and the relevant investigations were conducted as below:

- The bending deformation of the copter's arm when hovering at different arm length configurations.
- The step responses in the folded and unfolded processes of the copter's arm.

During the experiment, we found that the shape of the arm approximates straight before takeoff, and when the copter flies, the shape of the arm becomes the parabola-like due to the lifting force of the rotor, as illustrated in Figure 9. When the arm bends, the thrust T_i results in a deflection angle γ along the vertical direction, which makes the thrust T_i decomposed into a vertical component T_{ic} and a horizontal component T_{ir}. T_{ic} provides the lifting for the copter, while T_{ir} attempts to shrink the arm length and prevents the arm from extension (unfolding). As a result, the value of the angle γ plays an important role in the lifting and deformation performance of the copter. We hereby measured the unbending arm length before takeoff, which can be regarded as the actual arm length to calculate the angle γ in combination with the arm lengths measured during hover. Obviously, each arm length configuration corresponds to a special parabola. In order to calculate each angle γ, we first calculate the parabolic equation corresponding to each pair of actual and measured arm lengths.

Based on the prototype, Figure 10 shows the relationship between the arm length and the angle γ. It can be seen that the deflection angle γ decreases with the increase of the arm length, which roughly conforms to a quadratic curve. If aerodynamics is not taken into account, the longer the arm length, the smaller the T_i and T_{ir} of the copter during hover. Moreover, the range of the T_i varies from 0.319N to 0.323N, while the range of the T_{ir} varies from 0.035N to 0.061N. It is also found that the bending deformation of copter's arm has a little effect on lifting of copter, but it has obvious effect on the response speed of the deformable body frame due to it holds against unfolding of the arm.

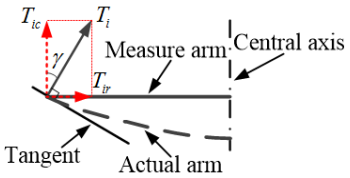

Figure 9. The bending deformation of the copter's arm during hover.

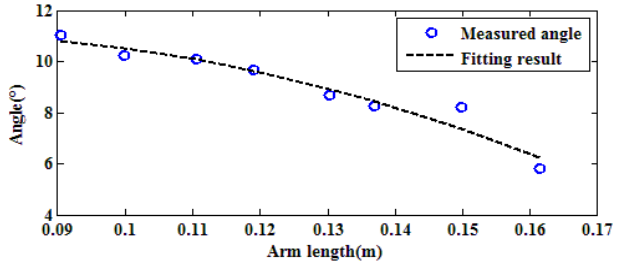

Figure 10. The variety of deflection angle with arm length during hover.

In addition, when the copter hovers, the step responses of the scalable arm's folded and unfolded processes were tested, respectively. In this test, the fully folded and unfolded configurations are set as shown in Figure 1(b) and (c)

respectively. The altitude reduction Δh caused by the folding and unfolding of the arm and the response time t required to fold and unfold the arm are two important measured indicators, as shown in TABLE 1, where the mean μ and standard deviation σ of Δh and t are shown for 10 trials.

Experimental results demonstrate that our scalable copter has a very fast response speed in both folding and unfolding. The response time t of folding is shorter than that of unfolding, which is partially contributed by horizontal component force T_{ir}. When folding, the altitude reduction Δh is larger than that of unfolding, which means that our copter is more stable when unfolding. However, the standard deviations σ of the two altitude reductions is a little larger than normal, which is that our current copter prototype can only supply a small lifting, so that a small voltage difference can lead to a significant difference in the altitude reduction. Therefore, it is necessary to manage the power output and noise for the copter in our future work.

TABLE I
ALTITUDE REDUCTION AND RESPONSE TIME IN THE STEP RESPONSE EXPERIMENTS OF THE ARM LENGTH FOLDED AND UNFOLDED

Deformation	t (seconds)		Δh (m)	
	μ	σ	μ	σ
Folded	0.20	0.01	0.155	0.072
Unfolded	0.35	0.02	0.016	0.010

C. Throwing

The copter's arm is usually fully folded in order to be stored easily during the absence of flight as shown in Figure 1(a), which is the similar as the bird folding wings during the rest. This inspires us to mimic flight behavior of birds using the scalable prototype. As the birds take off following the morphological adaptation, the morphing behavior, *i.e.* the wings folded and unfolded, can be mimicked by the deformation of the frame of the prototype. As a result, we designed a throwing experiment of our scalable copter, which can validate the dynamic characteristics of the scalable copter and meanwhile can mimic bird taking-off by using the deformation capability of the copter, as demonstrated in Figure 11. The three deformation states of our copter in this picture correspond to the three morphing states of birds respectively during takeoff.

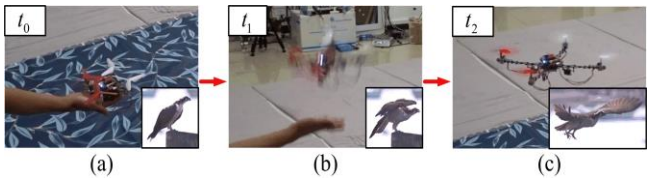

Figure 11. Copter's throwing inspried by bird take-off. (a) Fully folded configuration before take-off. (b) Semi-umfolded configuration allowing the rotors to start. (c) Unfolded configuration allowing the vehicle to hover stably.

Figure 12 plots the measured variety of arm length and altitude during throwing. The time t_0, t_1 and t_2 correspond to the three states shown in Figure 11. From Figure 12, we can also see that although the fully folded arm length during throwing is shorter than that in hover, the response speed is however decreased to 0.2s, which because the copter is in a low gravity during throwing and the horizontal component force T_{ir} is smaller than that in hover, and the friction effects between scalable arms and central body are less affected.

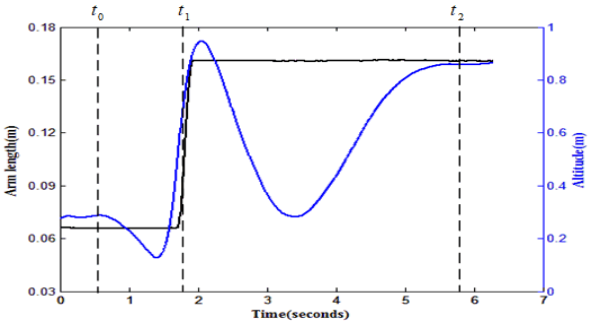

Figure 12. The variety of arm length and altitude during throwing.

D. Morphing Flying through a Narrow Window

We have successfully tested morphing flying through a narrow space of our copter, as shown in Figure 13. In this test, the narrow space is a square vertical window of 325×325mm. The results validate our copter has a fast actuation capability for large deformation, which indicates its excellent morphological adaptability.

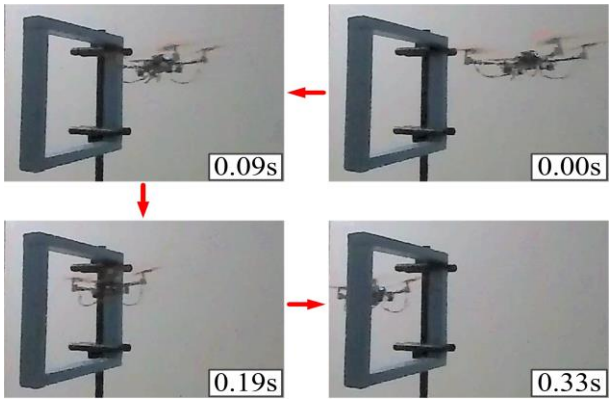

Figure 13. Morphing flying through a square vertical window of 325×325mm.

V. Conclusion

In this work, we presented a scalable multicopter whose controllably folding/unfolding mechanism is based on the novel SNIAE-SSE deformation mechanism. The advantages of the SNIAE-SSE mechanism consist of its single DOF and fast actuation capability as well as its large deformation ratio. Enabled by this SNIAE-SSE mechanism, a symmetrically and synchronously deformable quadcopter prototype was developed, its dynamics was then analyzed, and its dynamic characteristics during deformations in several flight missions were preliminarily validated. The results demonstrate that the new scalable multicopter can maintain stable flight behavior even the fast folding and unfolding body deformations are performed, which indicates its excellent capability of rapidly adapting to complex and dynamically changed environments. Ongoing research is to investigate its autonomous flight control under controllable deformations.

REFERENCES

[1] V. Kumar, and N. Michael, "Opportunities and Challenges With Autonomous Micro Aerial Vehicles," *Int. J. Rob. Res*., 31(11), pp. 1279–1291.

[2] D. Falanga , E. Mueggler , M. Faessler , and D. Scaramuzza, "Aggressive Quadrotor Flight through Narrow Gaps with Onboard Sensing and Computing using Active Vision," in *Robotics and Automation(ICRA),2017 IEEE International Conference on*. IEEE, 2017.

[3] S. Mintchev, L. Daler, G. L'Eplattenier, L. Saint-Raymond, and D. Floreano, "Foldable and self-deployable pocket sized quadrotor," in *Robotics and Automation(ICRA),2015 IEEE International Conference on*. IEEE, 2015, pp. 2190–2195.

[4] D. L. Yang, S. Mishra, D M. Aukes, and W. L. Zhang, "Design, Planning, and Control of an Origami-inspired Foldable Quad-rotor," in *American Control Conference (ACC)*, 2019.pp.2251-2256.

[5] C. Hintz, C. Torno, and L. R. G. Carrillo, "Design and dynamic modeling of a rotary wing aircraft with morphing capabilities," in *Unmanned Aircraft Systems (ICUAS), 2014 International Conference* on. IEEE, 2014, pp. 492–498.

[6] V. Riviere, A. Manecy, and S. Viollet, "Agile robotic fliers: A morphing-based approach," *Soft Robotics*, 2018.

[7] N. Bucki and M. W. Mueller, "Design and Control of a Passively Morphing Quadcopter," in *Robotics and Automation (ICRA), 2019 IEEE International Conference* on. IEEE, 2019, pp. 9116–9122.

[8] D. Falanga , K. Kleber , S. Mintchev , D. Floreano, and D Scaramuzza, "The Foldable Drone: A Morphing Quadrotor that can Squeeze and Fly," *IEEE Robotics and Automation Letters*, vol. 4, no. 2, pp.209-216, 2019.

[9] N. Zhao, Y. Luo, H. Deng, and Y. Shen, "The deformable quadrotor: Design, kinematics and dynamics characterization, and flight performance validation," in *Intelligent Robots and Systems (IROS), 2017 IEEE/RSJ International Conference* on. IEEE, 2017, pp. 2391–2396.

[10] N. Zhao, Y. Luo, H. Deng, and Y. Shen, "The Deformable Quad-Rotor: Mechanism Design, Kinematics, and Dynamics Effects Investigation," *Journal of Mechanisms and Robotics*, vol. 10, pp.1-5, 2018.

[11] K. Wohlhart. "Double-chain mechanism," in *Deployable Structures: Theory and Application, Proceedings of the IUTAM-IASS Symposium* on. 2000, pp. 457-466.

[12] D Mao, Y Luo, and Z You, "Planar closed loop double chain linkages," *Mechanism and Machine Theory*, vol. 44, no. 4, pp. 850-859, 2009.

[13] J Cai, X Deng, Y Xu, and J Feng, "Constraint Analysis and Redundancy of Planar Closed Loop Double Chain Linkages," *Advances in Mechanical Engineering*, vol. 6, pp. 635423, 2014.

[14] Z. You, S. Pellegrino. "Foldable bar structures," *International Journal of Solids & Structures*, vol. 34, no. 15, pp.1825-1847, 1997.

[15] N. Michael, D. Mellinger, Q. Lindsey, and V. Kumar, "The Grasp Multiple Micro-UAV Testbed," *IEEE Rob. Autom. Mag.*, vol. 17, no. 3, pp. 56–65, 2010.

[16] D. Mellinger, N. Michael, and V. Kumar, "Trajectory Generation and Control for Precise Aggressive Maneuvers With Quadrotors," *Int. J. Rob. Res.*, vol. 31, no. 5, pp. 664–674, 2012.

[17] K. H. Ang, G. Chong, Y. Li, "PID control system analysis, design, and technology," *IEEE Transactions on Control Systems Technology*, vol. 13, no. 4, pp. 559-576, 2005.

[18] A. Z. Azfar, D. Hazry, "A simple approach on implementing IMU sensor fusion in PID controller for stabilizing quadrotor flight control," in *Signal Processing & Its Applications (CSPA), 2011 IEEE 7th International Colloquium* on. IEEE, 2011, pp.28-32.